High-resolution tungsten spectroscopy relevant to the diagnostic of high-temperature tokamak plasmas

J. Rzadkiewicz,[2,*] Y. Yang,[1,†] K. Kozioł,[2] M. G. O'Mullane,[3] A. Patel,[4] J. Xiao,[1] K. Yao,[1] Y. Shen,[1] D. Lu,[1] R. Hutton,[1] Y. Zou,[1] and JET Contributors[‡]

[1]*Shanghai EBIT Laboratory, Key Laboratory of Nuclear Physics and Ion-Beam Application (MOE), Institute of Modern Physics, Fudan University, Shanghai 200433, China*
[2]*Narodowe Centrum Badań Jądrowych (NCBJ), Andrzeja Sołtana 7, 05-400 Otwock-Świerk, Poland*
[3]*Department of Physics, University of Strathclyde, Glasgow G4 0NG, United Kingdom*
[4]*Euratom/CCFE Fusion Association, Culham Science Centre, Abingdon, OX14 3DB, United Kingdom*

The x-ray transitions in Cu- and Ni-like tungsten ions in the 5.19–5.26 Å wavelength range that are relevant as a high-temperature tokamak diagnostic, in particular for JET in the ITER-like wall configuration, have been studied. Tungsten spectra were measured at the upgraded Shanghai- Electron Beam Ion Trap operated with electron-beam energies from 3.16 to 4.55 keV. High-resolution measurements were performed by means of a flat Si 111 crystal spectrometer equipped by a CCD camera. The experimental wavelengths were determined with an accuracy of 0.3–0.4 mÅ. The wavelength of the ground-state transition in Cu-like tungsten from the $3p^5 3d^{10} 4s 4d$ [(3/2,(1/2,5/2)$_2$)$_2$]$_{1/2}$ level was measured. All measured wavelengths were compared with those measured from JET ITER-like wall plasmas and with other experiments and various theoretical predictions including COWAN, RELAC, multiconfigurational Dirac-Fock (MCDF), and FAC calculations. To obtain a higher accuracy from theoretical predictions, the MCDF calculations were extended by taking into account correlation effects (configuration-interaction approach). It was found that such an extension brings the calculations closer to the experimental values in comparison with other calculations.

I. INTRODUCTION

The study of characteristic x-ray radiation emitted by highly ionized high-Z atoms is of great importance for both theoretical and applied atomic physics including fusion applications [1–3]. Measurements of such radiation can probe strong relativistic, quantum-electrodynamics (QED), and correlation effects. Neon-like and nickel-like heavy ions were proposed for x-ray lasing emission [4,5]. In fusion applications, spectral analysis of mid- and high-Z atomic systems is used to obtain key plasma parameters related to metallic impurity concentrations, ion and electron temperatures, plasma rotation velocity, and effective charge Z_{eff} [6–9].

The selection of tungsten as a plasma-facing material for the International Thermonuclear Experimental Reactor (ITER) has brought particular interest in its spectroscopic studies [10]. Recently, extensive experimental studies were performed on atomic structure and properties of x-ray transitions in tungsten, from lithium-like W^{71+} [2] through neon-like W^{64+}, potassium-like W^{55+} [11–14], nickel-like W^{46+} [3,15], and palladium-like W^{28+} [16,17] down to ytterbium-like W^{4+} tungsten [18]. Measurements of impurity x-ray spectra were also performed at the ASDEX Upgrade and JT60U tokamaks

for highly ionized tungsten ions up to Cu-like (W^{45+}) and Na-like (W^{63+}), respectively [19,20].

The experimental spectroscopic studies of tungsten ions were supported by extensive theoretical considerations (see, e.g., Ref. [21] and references therein). In the last few years a significant improvement has been achieved in the theoretical approaches, in particular by the development of large-scale relativistic configuration-interaction (CI) methods taking into account electron correlation effects. Such a technique was employed for $M1$ transitions in Ag-and Cd-like tungsten [17,22], electric-multipole transitions in Sn-like tungsten [23,24], and for transitions from low-lying levels in Ni-like tungsten [25]. An extended experimental and theoretical data base on the tungsten ions can be found in Refs. [26–28].

Recently, in measurements on the Joint European Torus (JET) with the ITER-like wall (ILW) configuration (beryllium wall and tungsten divertor) [29,30], the W^{45+} and W^{46+} ($3p$–$4d$) x-ray lines were observed. From analysis of tungsten line intensities, it was found that the W concentration is $\sim 10^{-5}$ for the ELMy H-mode JET plasmas (edge-localized-mode of plasma operation with high-energy confinement times) with 2.0–2.5 MA current, 2.7 T toroidal magnetic field and 14–18 MW neutral beam injection (NBI) power. Tungsten concentration determined from the W^{45+} line was systematically lower than that obtained from W^{46+} by $\sim 20\%$ for different types of JET discharges [7]. It was further shown that, in order to reproduce the experimental spectra in the 5.192–5.232 Å wavelength range at the measured electron

---

*jacek.rzadkiewicz@ncbj.gov.pl
†yangyang@fudan.edu.cn
‡See author list of "X. Litaudon *et al.*, Nucl. Fusion **97**, 102001 (2017)."

temperature $\sim$4 keV and density $\sim$3 $\times$ 10^{19} m^{-3}, it is necessary to perform advanced theoretical studies for the W ions considered, especially for those with open shells (e.g., W^{45+} and W^{47+}) [31,32].

Here we report on high-resolution measurements of Cu- and Ni-like tungsten spectra performed at the Shanghai Electron Beam Ion Trap (EBIT). Spectra relevant to the high-resolution x-ray diagnostic in JET were measured in the 5.19–5.26 Å wavelength region at the energies of the electron beam from 3.16 to 4.55 keV and compared with those measured at JET and with theoretical spectra calculated by advanced relativistic codes: FAC, utilizing the modified multiconfiguration Dirac–Hartree–Fock–Slater (DHFS, but commonly shortened to DHS) method and GRASP2K, utilizing the multi-configuration Dirac–Hartree–Fock (MCDHF, but commonly shortened to MCDF) method. To obtain high-accuracy theoretical predictions within the MCDF-CI method, large-scale CI calculations were performed.

II. ELECTRON BEAM ION TRAP EXPERIMENT

High-resolution x-ray measurements were performed at the upgraded Shanghai EBIT laboratory [33]. A general scheme of the experimental setup at the upgraded Shanghai EBIT is shown in Fig. 1. Tungsten was injected into EBIT by sublimation of tungsten hexacarbonyl W(CO)$_6$ through a gas injection system into the trapping region.

Highly ionized tungsten ions were produced by an electron quasimonoenergetic beams with energies set in a range from 3.16 to 4.55 keV and a current of 15–70 mA. These conditions correspond to electron densities of (2.5–11.6) $\times$ 10^{18} m^{-3}, as determined from the measurements of the diameters of the electron beam by the slit imaging system [34] (see Fig. 1) and from accurate measurements of the electron-beam energy and the current. The electron-beam diameter corresponding to electron densities at half maximum was found to be less than 70 μm. The full width of the electron-beam energy distribution at its half maximum was below 50 eV. The magnetic field in the central trap region was about 3 T. Table I shows the Shanghai EBIT operation parameters for the present set of experiments.
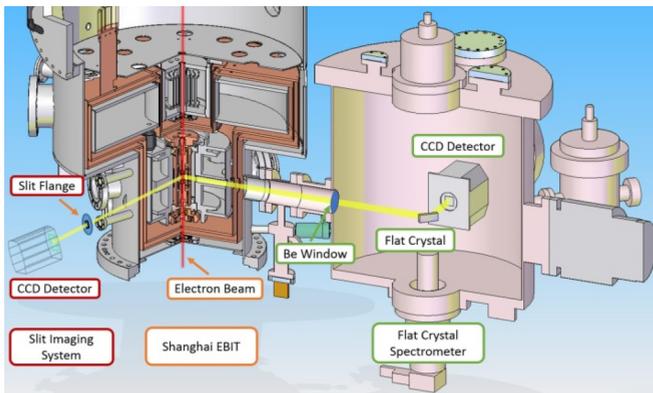
FIG. 1. A general scheme of the experimental setup at the upgraded Shanghai EBIT.

TABLE I. EBIT electron-beam parameters (energy, current, and corresponding electron density).

E_e (keV)	I_e (mA)	N_e (10^{18} m^{-3})
3.16	15	2.5
3.76	37	6.3
4.34	38	5.1
4.55	70	11.6

The x-ray spectra were registered by a flat-field spectrometer equipped with a Si 111 crystal with dimensions of 5.0 $\times$ 2.5 $\times$ 0.5 cm^3 and $2d = 6.2712$ Å [35] and a charge-coupled device (CCD) detector with 2048 $\times$ 2048 pixels (pixel size $\Delta x = 13.5$ μm). The resolving power of the spectrometer was found to be not worse than $\lambda / \Delta \lambda \approx 4200$ in the wavelength region of the investigation. The spectrometer was set to measure tungsten spectra in the wavelength range from 5.19 to 5.26 Å around the $\approx$56.5° Bragg angle. Data collection time was between 22 and 86 h per spectrum. Figure 2 shows tungsten spectra induced by electron beams at energies of 3.16, 3.76, 4.34, and 4.55 keV.
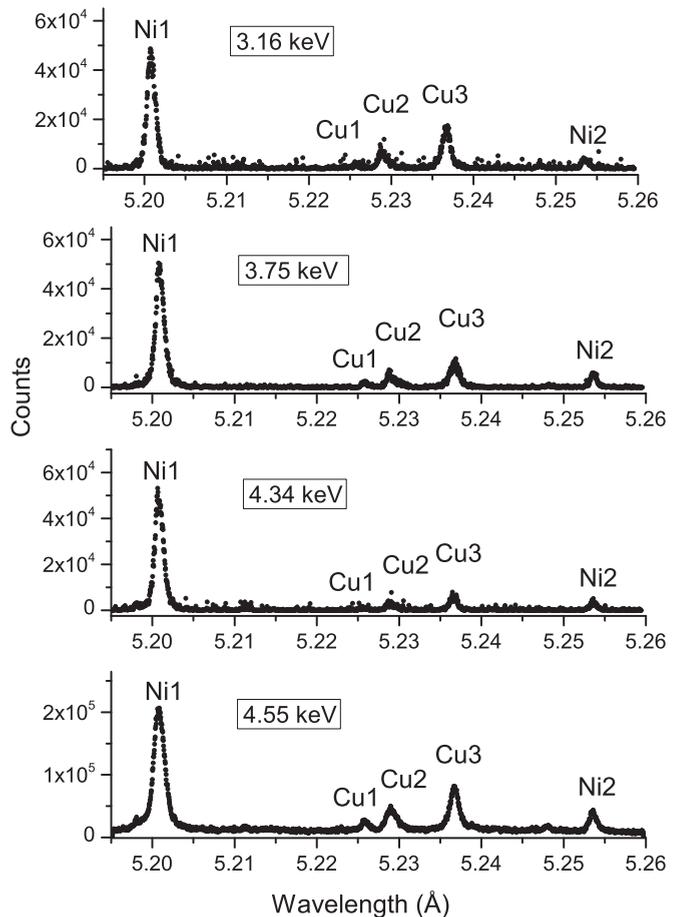
FIG. 2. X-ray spectra of Cu- and Ni-like tungsten ions measured on the upgraded Shanghai EBIT for electron-beam energies of 3.16, 3.76, 4.34, and 4.55 keV.
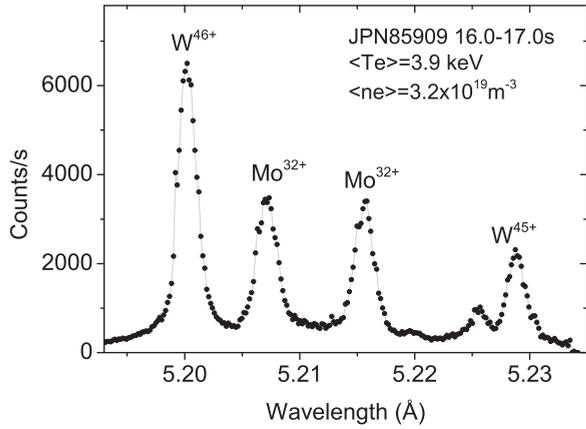
FIG. 3. Tungsten (W^{45+} and W^{46+}) and molybdenum (Mo^{32+}) x-ray lines observed in the spectrum measured at JET (shot #85909) at $T_e \approx 3.9$ keV and $n_e \approx 3.2 \times 10^{19}$ m^{-3}.

III. JOINT EUROPEAN TORUS MEASUREMENTS

The W^{45+} and W^{46+} ($3p$–$4d$) x-ray lines were observed at JET by means of an upgraded high-resolution x-ray spectrometer (KX1 diagnostic) in the wavelength region around 5.2 Å [36–38]. Figure 3 shows an example of such spectrum measured from typical steady-state ion cyclotron resonance frequency (ICRF) heated plasmas at JET shot #85909 in the time interval between 16 and 17 s. The corresponding electron density and temperature profiles measured by LIDAR Thomson scattering [39] are shown in Fig. 4 (together with fitting curves). It can be seen that both the electron temperature and density profiles are almost unchanged over the considered period of time in JET discharge #85909. The profiles correspond to the average electron temperature $\langle T_e \rangle = 3.9$ keV and density $\langle n_e \rangle = 3.2 \times 10^{19}$ m^{-3} of the JET plasmas on the magnetic axis.

By using the temperature and density profiles with ionization and recombination rates of W ions [19,40] one can estimate fractional abundance of tungsten ions. Figure 5 shows the fractional abundance under ionization equilibrium (JET shot #85909, time 16.0–17.0 s) for W^{44+}, W^{45+}, W^{46+}, and
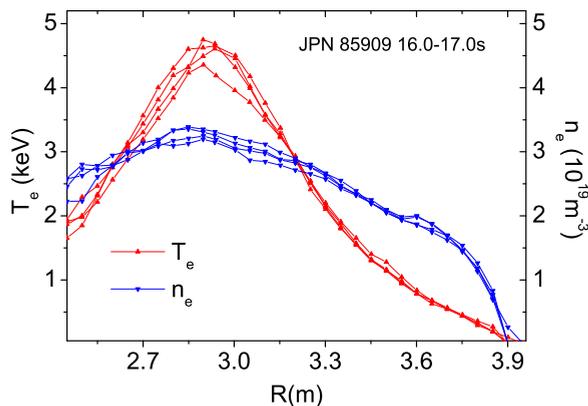
FIG. 4. Electron density and temperature profiles measured by LIDAR Thomson scattering at JET shot #85909 at a time between 16 and 17 s from the start of the discharge.
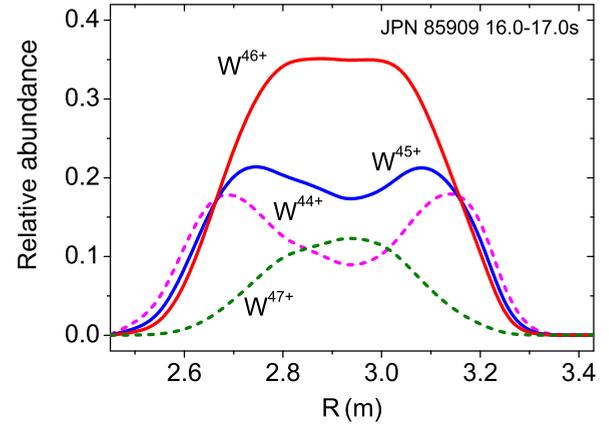
FIG. 5. Fractional abundance for W^{44+}–W^{47+} tungsten ions calculated for JET shot #85909 (time 16.0–17.0 s).

W^{47+} ions as a function of JET major radius (radial distance in meters from the main axis of JET torus). It can be seen that the W^{46+} and W^{45+} ions dominate over the other ionization stages of tungsten in the plasma core. The W^{46+} and W^{45+} fractional abundance increase toward the plasma core and have relatively broad maxima (in the case of W^{45+} ions, a slightly hollow structure can be observed). Thus, one can conclude that the x-ray emission from central regions of the JET plasma can be well described by considering only W^{46+} and W^{45+} lines.

IV. THEORETICAL CALCULATIONS

Transitions corresponding to the x-ray lines appearing in the spectra are described in Table II.

Calculations of radiative transition wavelengths were carried out with the GRASP2K [41,42] and FAC [43] codes. The GRASP2K code is based on the MCDF method, and FAC is based on the DHS method. The methodology of MCDF calculations performed in the present study is similar to that published earlier in many papers (see, e.g., Refs. [44–47]). The effective Hamiltonian for an N-electron system is expressed by

$$\hat{H} = \sum_{i=1}^{N} \hat{h}_D(i) + \sum_{j>i=1}^{N} C_{ij}, \qquad (1)$$

where $\hat{h}_D(i)$ is the Dirac operator for the ith electron and the terms C_{ij} account for electron-electron interactions. In general, the latter is a sum of the Coulomb interaction operator and the transverse Breit operator. An atomic state function (ASF) with the total angular momentum J and parity p is assumed in the

TABLE II. X-ray lines of Ni-and Cu-like tungsten ions observed in the 5.19–5.26 Å spectral range.

Line	Upper level		Lower level	
Ni1	$3p^5 3d^{10} 4d$ $(3/2,5/2)_1$		$3p^6 3d^{10}$	$^1S_0$
Cu1	$3p^5 3d^{10} 4s 4d$ $[(3/2,(1/2,5/2)_2]_{3/2}$		$3d^{10} 4s$	$^2S_{1/2}$
Cu2	$3p^5 3d^{10} 4s 4d$ $[(3/2,(1/2,5/2)_2]_{1/2}$		$3d^{10} 4s$	$^2S_{1/2}$
Cu3	$3p^5 3d^{10} 4s 4d$ $[(3/2,(1/2,5/2)_3]_{3/2}$		$3d^{10} 4s$	$^2S_{1/2}$
Ni2	$3p^5 3d^{10} 4d$ $(3/2,3/2)_1$		$3p^6 3d^{10}$	$^1S_0$

form

$$\Psi_s(JM^p) = \sum_m c_m(s)\Phi(\gamma_m JM^p), \qquad (2)$$

where $\Phi(\gamma_m JM^p)$ are the configuration state functions (CSFs), $c_m(s)$ are the configuration mixing coefficients for state s, and γ_m represents all information required to define a certain CSF uniquely. The CSFs are linear combinations of N-electron Slater determinants, which are antisymmetrized products of four-component Dirac orbital spinors. In the present calculations, the initial and final states of considered transitions were optimized separately, and the biorthonormal transformation was used [41]. Following this, the so-called relaxation effect was taken into account. In the GRASP2K code, the Breit interaction contribution to the energy was added as a perturbation, after the radial part of the wave function was optimized. In addition, two types of quantum electrodynamics (QED) corrections, self-energy (as screened hydrogenic approximation [48,49] of data of Mohr and coworkers [50]) and vacuum polarization (as potential of Fullerton an Rinker [51]), were included.

On the whole, the multiconfiguration DHS method is similar to the MCDF method, referring to effective Hamiltonian and multiconfigurational ASF. The main difference between the Dirac–Hartree–Fock method and the Dirac–Hartree–Fock–Slater method is that, in the (Dirac–)Hartree–Fock–Slater approach the nonlocal (Dirac–)Hartree–Fock exchange potential is approximated by a local potential. The FAC code uses an improved form of the local exchange potential (see Ref. [43] for details). The Breit contribution and leading QED contributions are also included in FAC calculations.

The accuracy of the wave function depends on the CSFs included in its expansion [52,53]. The accuracy can be improved by extending the CSF set with the CSFs corresponding to excitations from orbitals occupied in the multireference CSF set (MR) to unfilled orbitals of the active orbital set (i.e., CSFs for virtual excited states). The CI method makes it possible to include the major part of the electron correlation contribution in the energy of atomic levels. The CI approach requires the choice of a proper basis of CSFs for the virtual excited states. It is reached by systematic building of CSF sequences by extending the active space (AS) of orbitals and monitoring concurrently the convergence of self-consistent calculations [17,52,54]. In the present work, large-scale MCDF-CI calculations were performed to provide theoretical predictions of Ni- (W^{46+}) and Cu-like (W^{45+}) line wavelength in the 5.19–5.26 Å region.

Table III shows the numbers of CSFs in different active spaces used for upper and lower states in calculations of the $|[Mg]3p^53d^{10}4d^1\rangle_{J=1} \rightarrow |[Mg]3p^63d^{10}\rangle_{J=0}$ transitions in Ni-like (W^{46+}) and $|[Mg]3p^53d^{10}4s^14d^1\rangle_{J=1/2,3/2} \rightarrow |[Mg]3p^63d^{10}4s^1\rangle_{J=1/2}$ transitions in Cu-like (W^{45+}) tungsten ions. Some CSFs are excluded by using the *jjreduce3* program, a part of the GRASP2K program set. In this way, the number of CSFs was reduced by up to 35%. The MR set (labeled as AS0) represents the $[Mg]3p^53d^{10}4d^1$ upper and $[Mg]3p^63d^{10}$ lower states of transitions in W^{46+} and $[Mg]3p^53d^{10}4s^14d^1$ upper and $[Mg]3p^63d^{10}4s^1$ lower states of transitions in W^{45+}.

Table IV lists the theoretical wavelengths of the Ni1, Ni2, Cu1, Cu2, and Cu3 lines for the following extensions of our

TABLE III. Numbers of CSFs for different active spaces used in calculations of considered transitions in Ni- and Cu-like tungsten ions.

| Stage | Model | Number of CSFs (reduced) | |
		Upper states	Lower state
W^{46+}			
	AS0	3	1
	AS1	8845	302
	AS2	58344	1417
	AS3	152800	3370
	AS4	292213	6161
W^{45+}			
	AS0	11	1
	AS1	4571	77
	AS2	26594	362
	AS3	68624	866
	AS4	130661	1589

calculations. In the first step we have calculated the wavelengths by means of the pure Dirac–Fock approach followed by Breit and QED corrections (the first three rows in Table IV). The Breit and QED contributions shift the considered tungsten lines by about 10 mÅ and 1 mÅ, respectively.

In the present paper, the following active spaces of virtual orbitals were taken into account: AS1 containing subshells with $n = 4$ and $l = 0$–3, AS2 for subshells with $n = 4$–5 and $l = 0$–4, AS3 for subshells with $n = 4$–6 and $l = 0$–4, and AS4 for subshells with $n = 4$–7 and $l = 0$–4. For W^{46+} we considered all possible single (S) and double (D) substitutions from $3s$, $3p$, $3d$, $4d$ occupied subshells. In this case, the inactive core contains $1s$, $2s$, and $2p$ subshells. Because the size of expansions increases with the size of the MR set, for W^{45+} we used another model, which is a common approach (see e.g., Refs. [17,55]). The occupied subshells were divided into three kinds: inactive core, active core (C), and valence (V) subshells. All open subshells (i.e., $3p$, $4s$, and $4d$ for upper states of transitions and $4s$ for lower state) are considered as valence subshells. The $n = 1$, 2 subshells are an inactive core and the $n = 3$ subshells are an active core. Then, for W^{45+} we considered SD substitutions divided into two groups: VV (both substituted electrons are from valence subshells) and CV (first substituted electron is from a valence subshell and the other is from an active core subshell).

TABLE IV. Wavelengths (in Å) of transitions in Cu-like (W^{45+}) and Ni-like (W^{46+}) from different theoretical GRASP2K calculations. Transition labels are explained in Table II.

Calculation		Ni1	Ni2	Cu1	Cu2	Cu3
DF		5.1831	5.2383	5.2067	5.2091	5.2191
+ Breit		5.1938	5.2476	5.2170	5.2198	5.2299
+ QED		5.1947	5.2486	5.2178	5.2207	5.2308
+ CI:	AS1	5.1698	5.2224	5.2207	5.2242	5.2326
	AS2	5.1959	5.2484	5.2214	5.2246	5.2333
	AS3	5.1994	5.2518	5.2246	5.2276	5.2365
	AS4	5.1994	5.2517	5.2251	5.2280	5.2370

As described above, the correlation effects were included by taking into consideration SD electron replacements within an active set of virtual orbitals (with a restricted number of CSFs for Cu-like open-shell configurations). The wavelengths calculated in the extension within the active set up to $n = 7$ are higher from the MR values (DF + Breit + QED) by 2.3–4.7 mÅ. With this theoretical approach, a good convergence was obtained for both the Cu- and Ni-like ions.

V. RESULTS AND DISCUSSION

As shown in Sec. II, we studied four EBIT spectra of W ions over the wavelength range from 5.19 to 5.26 Å for electron-beam energies from 3.16 to 4.55 keV. In the spectra for these electron-beam energies, the ground-state transitions from $3p^5 3d^{10} 4s4d$ states of W^{45+} and $3p^5 3d^{10} 4d$ ones of W^{46+} ions appeared (see Fig. 2). For all considered electron-beam energies, the Ni1 ($4d_{5/2} \rightarrow 3p_{3/2}$) transition dominates over the others (Cu1, Cu2, Cu3 and Ni2). The relative contribution from the radiation emitted by Cu-like W^{45+} ions decreases with the increase of the electron-beam energy because of the lower ionization potential of Cu-like tungsten W^{45+} (2.43 keV) in comparison with Ni-like tungsten (4.06 keV) [5].

After the line identification it was possible to perform the wavelength calibration. Because the investigated spectral range was very narrow (5.19–5.26 Å), a linear relationship between detector channel (pixel) numbers and wavelengths was adopted. In the first step, the reference NIST wavelengths for Cu- and Ni-like transitions [15,21] were assigned to the fitted peak centroids obtained from the Gaussian fits for each measured spectrum. It was found that the linear relations between pixel numbers (1–2048) and wavelengths produce a large coefficient of determination ($R^2 > 0.9988$) that measures how close the fitted curve is to the measured data points. It is worth mentioning that an introduction of a quadratic factor to the pixel-number–wavelength relationship does not improve the R^2 value. By comparing the reference NIST values for Ni1 and Ni2 lines (that serve as our spectral range limits) and corresponding wavelengths obtained from the linear fit [$f(x_i) = ax_i + b$ where x_i is a pixel number], we have estimated the spectral range accuracy (a relative spectrometer calibration error) to be 0.3 mÅ. After this step of the calibration procedure we have obtained a wavelength "measuring line" with precisely known regular intervals ($\Delta x = \Delta \lambda$).

Having a relative linear calibration of the spectrometer, the absolute calibration requires only measurements of a single reference line in the spectral range of interest. In our case, we have measured the Ly-$\beta_{1,2}$ ($3p_{3/2}$-$1s$ and $3p_{1/2}$-$1s$) lines of H-like Si ions. The wavelengths of hydrogen-like lines are used as high-precision, absolute, and calculable atomic x-ray standards, because their spectral purity and satellite-free structure (see, e.g., Ref. [59]). The calibration measurement was performed at the electron-beam energy of 4.6 keV and a current of 70 mA. By assigning the theoretical values of Ly-β_1 (5.217960 Å) and Ly-β_2 (5.216819 Å) calculated by means of the MCDFGME code [60] to the pixel numbers (Gaussian peak centroids determined with the accuracy that corresponds to 0.023 mÅ and 0.044 mÅ wavelength accuracy) we have obtained the absolute calibration. To estimate the uncertainty

TABLE V. Wavelengths (λ_{expt}) of the Ni-like lines measured at various electron-beam energies (E_e) and average values (λ_{avg}).

| Line | λ_{expt} (Å) at E_e (keV) | | | | λ_{avg} (Å) |
	3.16	3.76	4.34	4.55	
Ni1	5.20077	5.20077	5.20076	5.20071	5.2008(3)
Ni2	5.25403	5.25404	5.25404	5.25396	5.2540(3)
Uncertainty contributions:					
Statistics					<0.03 mÅ
Spectrometer calib.					0.30 mÅ
Reference					0.022 mÅ
Ref. statistics					0.045 mÅ

of the theoretical reference wavelengths we have compared our Ly-$\beta_{1,2}$ wavelength calculations with the current NIST ASD data that are reported with the uncertainty of 0.022 mÅ [61]. An agreement between both calculations within the reported uncertainty (0.022 mÅ) was found. Therefore, this value was taken as the uncertainty of our theoretical reference values.

The measured wavelengths of the Ni1, Ni2, Cu1, Cu2, and Cu3 lines are listed in Tables V and VI together with uncertainty contributions for all spectra (3.16, 3.76, 4.34, and 4.55 keV). The wavelengths of Cu- and Ni-like tungsten lines were determined by means of multipeak Gaussian function fits with a linear background. The determined line wavelengths from all beam energies were averaged and are presented in the last column of Tables V and VI and in Table VII with the total uncertainties of 0.3–0.4 mÅ. In comparison with NIST experimental values [15,21] the experimental uncertainties were reduced by at least factor of three (see Table VII). To the best of our knowledge, it is the most accurate measurement in this wavelength range presented so far for Cu- and Ni-like tungsten ions. Moreover, the wavelength of the Cu1 line [$3p^5 3d^{10} 4s4d$ $(3/2,2)_{3/2} \rightarrow 3d^{10} 4s$ $^2S_{1/2}$] was measured for the first time. One can see in Tables V and VI that the dominant contribution to the measured uncertainties originates from the relative spectrometer calibration. The crystal dispersion errors, determined by using the XOP code [62], are negligible

TABLE VI. Wavelengths (λ_{expt}) of the Cu-like lines measured at various electron-beam energies E_e and average values (λ_{avg}).

| Line | λ_{expt} (Å) at E_e (keV) | | | | λ_{avg} (Å) |
	3.16	3.76	4.34	4.55	
Cu1	5.22595	5.22592	5.22590	5.22602	5.2259(4)
Cu2	5.22913	5.22913	5.22919	5.22926	5.2292(3)
Cu3	5.23697	5.23696	5.23689	5.23696	5.2369(3)
Uncertainty contributions:					
Statistics Cu1					<0.20 mÅ
Statistics Cu2,3					<0.10 mÅ
Spectrometer calib.					0.30 mÅ
Reference					0.022 mÅ
Ref. statistics					0.045 mÅ

TABLE VII. Ground-state transitions in $W^{45+,46+}$ in the 5.19–5.26 Å wavelength range.

| Line | Theory | | | | | Expt. | | NIST[a,b] |
	MCDF	MCDF-CI	FAC	RELAC[c]	COWAN[a]	Present EBIT	Other	
Ni1	5.1947[d]	5.1994[d]	5.1959[d]	5.1944	5.218	5.2008(3)[d]	5.2002(9)[e]	5.2004(9)
	5.1942[f]		5.1963[g]				5.203(3)[h]	
							5.203(3)[i]	
							5.199(9)[j]	
							5.2005(9)[d,k]	
Cu1	5.2179[d]	5.2251[d]	5.2191[d]			5.2259(4)[d]	5.2263(9)[d,k]	
			5.2197[g]					
Cu2	5.2207[d]	5.2280[d]	5.2218[d]	5.2192	5.230	5.2292(3)[d]	5.2295(9)[d,k]	5.2289(11)
			5.2230[g]					
Cu3	5.2308[d]	5.2370[d]	5.2316[d]	5.2298	5.241	5.2369(3)[d]	5.238(9)[j]	5.2379(17)
			5.2313[g]					
Ni2	5.2486[d]	5.2517[d]	5.2500[d]		5.272	5.2540(3)[d]	5.2520(16)[e]	5.2533(9)
	5.2472[f]		5.2495[g]				5.255(3)[i]	

[a]Neill *et al.* [15]; [b]Kramida [21]; [c]Fournier [26]; [d]This work; [e]Clementson *et al.* [56]; [f]Dong *et al.* [25]; [g]Clementson *et al.* [28]; [h]Ralchenko *et al.* [3]; [i]Tragin *et al.* [57]; [j]Osborne *et al.* [58]; [k]JET.

(0.012 mÅ) in comparison with the reference and statistics errors. The crystal dispersion errors were determined for a 0.5-cm-thick Si (111) crystal within a flat perfect crystal model in a Bragg diffraction geometry as a difference of the rocking curve centroids (average values for s- and p-polarization planes) calculated for two extreme wavelengths of our spectral range (Ni1 and Ni2).

In Table VII we present the experimental wavelengths of the Ni1, Cu1, and Cu2 tungsten lines determined from JET measurements performed with the upgraded high-resolution x-ray diagnostic $\lambda/\Delta\lambda > 1.2 \times 10^4$ [31–33]. The wavelengths were determined as average values from spectra taken from plasma JET shot #85909 at 1 s time intervals at times between 10 and 17 s from the beginning of the discharge. The JET spectra were also fit by multipeak Gaussian functions with a linear background. The JET spectra can be affected by the Doppler shift due to the tokamak toroidal rotation. For the ICRF-heated JET plasmas toroidal rotation should not exceed ∼20 krad/s [63]. For the plasma JET shot #85909 the average ICRF heating power was below 4 MW. It was found that for such a heating the toroidal angular frequency for the JET central plasma does not exceed 10 krad/s [64,65], which corresponds to maximum Doppler shifts of 0.7 and 0.8 mÅ values for Mo^{32+} and $W^{45+,46+}$ lines, respectively.

To calibrate the JET spectra we assumed the same toroidal rotation for tungsten and molybdenum ions and performed the wavelength calibration by means of the $E1$ and $M2$ lines of Mo^{32+} (5.2076 and 5.2162 Å) originating from the molybdenum impurity in JET plasmas [7,32]. To verify this assumption, we estimated the possible difference between the toroidal angular frequencies (and corresponding Doppler shifts) for Mo^{32+} and $W^{45+,46+}$ ions. If we assume that toroidal rotations would be different for Mo^{32+} and $W^{45+,46+}$ ions by about 5 krad/s (that seems to be the upper limit) the corresponding Doppler shifts of Mo^{32+} and $W^{45+,46+}$ lines would differ by no more than 0.5 mÅ. We took this value as a maximum uncertainty of our calibration procedure related to the Doppler shifts. The calibration wavelengths of Mo^{32+}

lines were calculated by using the MCDF-CI method. The uncertainties of the reference wavelengths were estimated by comparing our calculations with those obtained from relativistic many-body perturbation theory [66] and the experimental value (for the $E1$ transition) recommended by NIST [67]. As the uncertainty of the reference wavelength, we conservatively took the maximum difference between experimental and theoretical results, which is 0.7 mÅ. One should also point out that, in our analysis, we disregarded the experimental wavelengths obtained at the Alcator C and Alcator C-Mod tokamaks [68] because these values appear to be systematically shifted towards lower wavelengths by 1–2 mÅ, possibly due to the Doppler shift. The wavelengths of the Ni1 and Cu1, Cu2 tungsten lines determined from the JET spectra are presented in Table VII with total uncertainties of 0.9 mÅ. The main contribution to the total uncertainty estimate comes from the Doppler shift correction (with a 0.5 mÅ uncertainty) and the $E1$ and $M2$ Mo^{32+} reference wavelengths (0.7 mÅ). One can clearly see that the wavelengths measured at JET are in an excellent agreement (∼0.3–0.5 mÅ) with values measured in the EBIT.

In Table VII the experimental wavelengths are compared with the MR MCDF (marked simply as MCDF for clarity), MCDF-CI, FAC, RELAC [69], and COWAN [70] theoretical predictions. The MCDF, FAC, and RELAC calculations based on the fully relativistic approach agree much better with experiment than those obtained by the COWAN code. This observation is consistent with that presented in other studies (see, e.g., Ref. [15]).

The differences between the theoretical and experimental wavelengths of Ni- and Cu-like lines are in the range of (4–10) mÅ when just the participating configurations are considered in the calculation. To reproduce the experimental wavelengths more accurately, we applied the high-accuracy MCDF-CI calculations taking into account the correlations effects by implementing SD virtual excitations from the core and valence shells (see Sec. IV for details). Figures 6 and 7 show the convergence behavior of theoretical predictions for the Ni1,
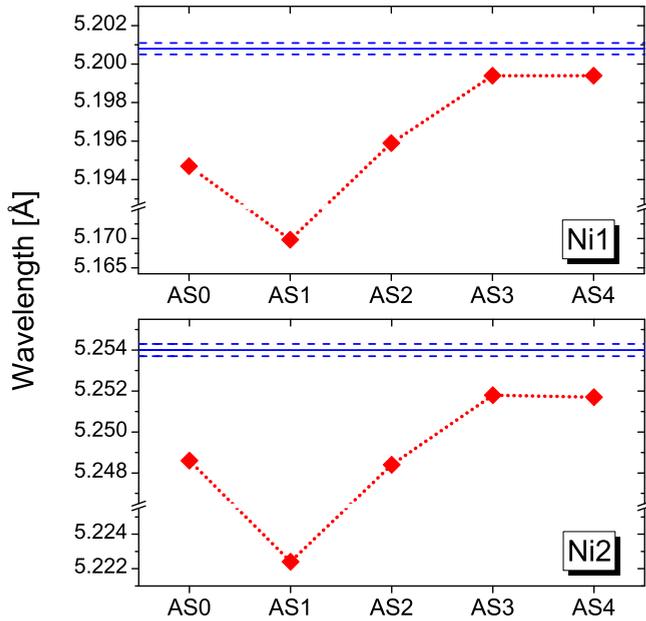
FIG. 6. The MCDF-CI wavelength calculations for the Ni1 (upper) and Ni2 (bottom) tungsten lines as a function of the active set (ASn) compared with the experimental values. The dotted lines with diamond symbols represent the MCDF-CI calculations, while solid and dashed lines show the experimental values and their uncertainties.
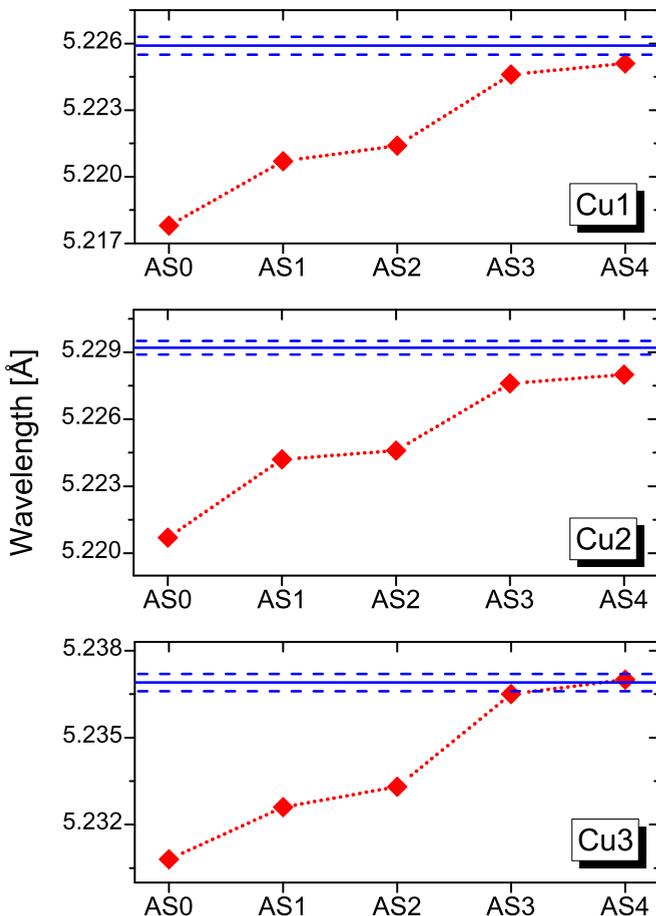
FIG. 7. Same as Fig. 6 but for Cu1, Cu2, and Cu3 tungsten lines.
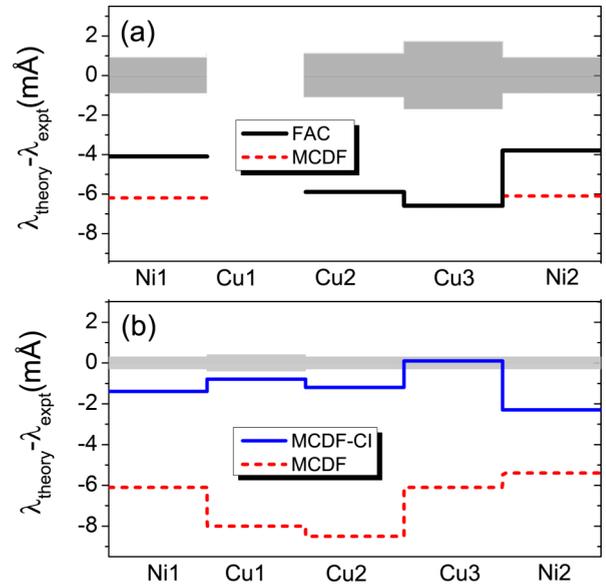
FIG. 8. Comparison of (a) previous and (b) present theoretical and experimental wavelengths of Ni1, Ni2 and Cu1, Cu2, Cu3 lines. The previous experimental wavelengths are taken from Refs. [15,21], while the theoretical ones were taken from Refs. [25,28]. The experimental uncertainties are represented by shaded area.

Ni2 and Cu1, Cu2, Cu3 line wavelengths as a function of the active set (ASn) together with the experimental values. It is worth mentioning that, for the AS1 active set containing virtual excitations to subshells with $n = 4$ and $l = 0$–3, one can observe a significant drop of the calculated wavelengths to ~5.17 and ~5.22 Å for Ni1 and Ni2 wavelengths, respectively (see Fig. 6). The calculations for the active sets with a higher n quantum number in the active set (and higher number of CSFs) show a significant increase of the wavelengths toward experimental values of the Cu1, Cu2, Cu3 and Ni1, Ni2 lines. An increase of the wavelength values within the AS3 and AS4 active sets is about 3–7 mÅ in comparison with the MR values. A convergence is reached for the AS3 and AS4 active sets ($n \geqslant 6$) for both the Cu- and Ni-like tungsten calculations.

An improvement of the experimental precision and theoretical predictions taking into account correlation effects is illustrated in Fig. 8. A significant underestimation of previous experimental Cu2, Cu3 and Ni1, Ni2 wavelengths by MCDF and FAC theoretical predictions is shown in Fig. 8(a). Figure 8(b) clearly shows not only an improvement of the experimental wavelength precision (to 0.3–0.4 mÅ uncertainty values), but also presents a much better agreement between our theoretical predictions and new experimental results. The most accurate MCDF-CI calculations (with SD substitutions up to $n = 7$) reduce the discrepancies between theory and experiment below 1.5 mÅ for Ni1 and Cu1, Cu2, Cu3 and below 2.5 mÅ for Ni2, respectively.

VI. SUMMARY

High-resolution measurements of Cu- and Ni-like tungsten wavelengths were performed in the 5.19–5.26 Å range at the upgraded Shanghai EBIT. Spectra were produced by an

electron beam with energies from 3.16 to 4.55 keV. The Cu- and Ni-like tungsten lines were measured with a significantly better precision (0.3–0.4 mÅ) in comparison with previous measurements (0.9–1.7 mÅ). Moreover, the wavelength of the ground-state transition in Cu-like tungsten from the $3p^5 3d^{10} 4s 4d$ $[(3/2, (1/2, 5/2)_2]_{3/2}$ level (Cu1 line) was measured.

The measurements were performed in the spectral range that is relevant to tokamak plasma diagnostics, in particular to the high-resolution x-ray diagnostic operated at JET. The Ni- and Cu-like wavelengths determined from JET spectra are in excellent agreement (0.3–0.5 mÅ) with values measured at the Shanghai EBIT.

It was also shown that previous calculations significantly underestimate the experimental values of Cu- and Ni-like tungsten wavelengths in the considered spectral range. Our extended MCDF calculations taking into account the correlation effects within an active set with quantum number up to $n \leqslant 7$ reduce the underestimation to less than 2.5 mÅ. Results of this study provide an important benchmark for x-ray measurements in tokamaks, in particular for JET and ITER.

[1] J. D. Gillaspy, J. Instrum. **5**, C10005 (2010).

[2] Y. Podpaly, J. Clementson, P. Beiersdorfer, J. Williamson, G. V. Brown, and M. F. Gu, Phys. Rev. A **80**, 052504 (2009).

[3] Yu. Ralchenko, J. N. Tan, J. D. Gillaspy, J. M. Pomeroy, and E. Silver, Phys. Rev. A **74**, 042514 (2006).

[4] D. J. Fields, R. S. Walling, G. M. Shimkaveg, B. J. MacGowan, L. B. Da Silva, J. H. Scofield, A. L. Osterheld, T. W. Phillips, M. D. Rosen, D. L. Matthews, W. H. Goldstein, and R. E. Stewart, Phys. Rev. A **46**, 1606 (1992).

[5] S. R. Elliott, P. Beiersdorfer, B. J. MacGowan, and J. Nilsen, Phys. Rev. A **52**, 2689 (1995).

[6] P. Beiersdorfer, J. Clementson, J. Dunn, M. F. Gu, K. Morris, Y. Podpaly, E. Wang, M. L. Bitter, R. Feder, K. W. Hill, D. Johnson, and R. Barnsley, J. Phys. B: At., Mol. Opt. Phys. **43**, 144008 (2010).

[7] T. Nakano, A. E. Shumack, C. F. Maggi, M. Reinke, K. D. Lawson, I. Coffey, T. Pütterich, S. Brezinsek, B. Lipschultz, G. F. Matthews, M. Chernyshova, K. Jakubowska, M. Scholz, J. Rzadkiewicz, T. Czarski, W. Dominik, G. Kasprowicz, K. Pozniak, W. Zabolotny, K.-D. Zastrow, and N. J. Conway, J. Phys. B: At., Mol. Opt. Phys. **48**, 144023 (2015).

[8] K. W. Hill, M. L. Bitter, S. D. Scott, A. Ince-Cushman, M. Reinke, J. E. Rice, P. Beiersdorfer, M. F. Gu, S. G. Lee, C. Broennimann, and E. F. Eikenberry, Rev. Sci. Instrum. **79**, 10E320 (2008).

[9] A. Czarnecka, K.-D. Zastrow, J. Rzadkiewicz, I. H. Coffey, K. D. Lawson, and M. G. O'Mullane, Plasma Phys. Control. Fusion **53**, 035009 (2011).

[10] C. H. Skinner, Phys. Scr. **T134**, 014022 (2009).

[11] C. Biedermann, R. Radtke, R. Seidel, and T. Pütterich, Phys. Scr. **T134**, 014026 (2009).

[12] Yu. Ralchenko, I. N. Draganic, J. N. Tan, J. D. Gillaspy, J. M. Pomeroy, J. Reader, U. Feldman, and G. E. Holland, J. Phys. B: At., Mol. Opt. Phys. **41**, 021003 (2008).

[13] J. Clementson and P. Beiersdorfer, Phys. Rev. A **81**, 052509 (2010).

[14] P. Beiersdorfer, J. K. Lepson, M. B. Schneider, and M. P. Bode, Phys. Rev. A **86**, 012509 (2012).

[15] P. Neill, C. Harris, A. S. Safronova, S. Hamasha, S. Hansen, U. I. Safronova, and P. Beiersdorfer, Can. J. Phys. **82**, 931 (2004).

[16] C. S. Harte, C. Suzuki, T. Kato, H. A. Sakaue, D. Kato, K. Sato, N. Tamura, S. Sudo, R. D'Arcy, E. Sokell, J. White, and G. O'Sullivan, J. Phys. B: At., Mol. Opt. Phys. **43**, 205004 (2010).

[17] Z. Fei, R. Zhao, Z. Shi, J. Xiao, M. Qiu, J. Grumer, M. Andersson, T. Brage, R. Hutton, and Y. Zou, Phys. Rev. A **86**, 062501 (2012).

[18] J. Clementson, P. Beiersdorfer, E. W. Magee, H. S. McLean, and R. D. Wood, J. Phys. B: At., Mol. Opt. Phys. **43**, 144009 (2010).

[19] T. Pütterich, R. Neu, R. Dux, A. D. Whiteford, M. G. O'Mullane, and A. U. Team, Plasma Phys. Control. Fusion **50**, 085016 (2008).

[20] J. Yanagibayashi, T. Nakano, A. Iwamae, H. Kubo, M. Hasuo, and K. Itami, J. Phys. B: At., Mol. Opt. Phys. **43**, 144013 (2010).

[21] A. Kramida, Can. J. Phys. **89**, 551 (2011).

[22] X.-B. Ding, F. Koike, I. Murakami, D. Kato, H. A. Sakaue, C.-Z. Dong, N. Nakamura, A. Komatsu, and J. Sakoda, J. Phys. B: At., Mol. Opt. Phys. **44**, 145004 (2011).

[23] G. Gaigalas, Z. Rudzikas, E. Gaidamauskas, P. Rynkun, and A. Alkauskas, Phys. Rev. A **82**, 014502 (2010).

[24] G. Gaigalas, Z. Rudzikas, P. Rynkun, and A. Alkauskas, Phys. Rev. A **83**, 032509 (2011).

[25] C.-Z. Dong, S. Fritzsche, and L. Y. Xie, J. Quant. Spectrosc. Radiat. Transfer **76**, 447 (2003).

[26] K. Fournier, At. Data Nucl. Data Tables **68**, 1 (1998).

[27] A. E. Kramida and T. Shirai, At. Data Nucl. Data Tables **95**, 305 (2009).

[28] J. Clementson, P. Beiersdorfer, T. Brage, and M. F. Gu, At. Data Nucl. Data Tables **100**, 577 (2014).

[29] F. Romanelli, Nucl. Fusion **53**, 104002 (2013).

[30] G. F. Matthews, P. Edwards, T. Hirai, M. Kear, A. Lioure, P. Lomas, A. Loving, C. Lungu, H. Maier, P. Mertens, D. Neilson, R. Neu, J. Pamela, V. Philipps, G. Piazza, V. Riccardo, M. Rubel, C. Ruset, E. Villedieu, M. Way, and I.-l. W. P. Team, Phys. Scr. **T128**, 137 (2007).

[31] K. Słabkowska, M. Polasik, E. Szymańska, J. Starosta, Ł. Syrocki, J. Rzadkiewicz, and N. R. Pereira, Phys. Scr. **T161**, 014015 (2014).

[32] K. Słabkowska, J. Rzadkiewicz, Ł. Syrocki, E. Szymańska, A. E. Shumack, M. Polasik, N. R. Pereira, and J. Contributors, J. Phys. B: At., Mol. Opt. Phys. **48**, 144028 (2015).

[33] D. Lu, Y. Yang, J. Xiao, Y. Shen, Y. Fu, B. Wei, K. Yao, R. Hutton, and Y. Zou, Rev. Sci. Instrum. **85**, 093301 (2014).

[34] Y. Yang, D. Lu, Y.-Q. Fu, K. Yao, W.-D. Chen, J. Xiao, Z.-X. Geng, and Y.-M. Zou, Chin. Phys. B **20**, 080701 (2011).

[35] J. H. Underwood, in *X-Ray Data Booklet*, 3rd ed. (Lawrence Berkeley National Laboratory, Berkeley, 2009), Chap. 4.1., http://cxro.lbl.gov/x-ray-data-booklet.

[36] J. Rzadkiewicz, W. Dominik, M. Scholz, M. Chernyshova, T. Czarski, H. Czyrkowski, R. Dabrowski, K. Jakubowska, L. Karpinski, G. Kasprowicz, K. Kierzkowski, K. Pozniak, Z. Salapa, W. Zabolotny, P. Blanchard, S. Tyrrell, and K.-D. Zastrow, Nucl. Instrum. Methods Phys. Res., Sect. A **720**, 36 (2013).

[37] M. Chernyshova, T. Czarski, W. Dominik, K. Jakubowska, J. Rzadkiewicz, M. Scholz, K. Pozniak, G. Kasprowicz, and W. Zabolotny, J. Instrum. **9**, C03003 (2014).

[38] A. E. Shumack, J. Rzadkiewicz, M. Chernyshova, K. Jakubowska, M. Scholz, A. Byszuk, R. Cieszewski, T. Czarski, W. Dominik, L. Karpinski, G. Kasprowicz, K. Pozniak, A. Wojenski, W. Zabolotny, N. J. Conway, S. Dalley, J. Figueiredo, T. Nakano, S. Tyrrell, K.-D. Zastrow, and V. Zoita, Rev. Sci. Instrum. **85**, 11E425 (2014).

[39] C. W. Gowers, B. W. Brown, H. Fajemirokun, P. Nielsen, Y. Nizienko, and B. Schunke, Rev. Sci. Instrum. **66**, 471 (1995).

[40] H. P. Summers, The ADAS User Manual, version 2.6 (2004).

[41] P. Jönsson, X. He, C. Froese Fischer, and I. P. Grant, Comput. Phys. Commun. **177**, 597 (2007).

[42] P. Jönsson, G. Gaigalas, J. Bieroń, C. Froese Fischer, and I. P. Grant, Comput. Phys. Commun. **184**, 2197 (2013).

[43] M. F. Gu, Can. J. Phys. **86**, 675 (2008).

[44] K. G. Dyall, I. P. Grant, C. Johnson, F. A. Parpia, and E. Plummer, Comput. Phys. Commun. **55**, 425 (1989).

[45] I. P. Grant, *Relativistic Quantum Theory of Atoms and Molecules*, edited by I. P. Grant, Springer Series on Atomic, Optical, and Plasma Physics Vol. 40 (Springer, New York, 2007).

[46] M. Polasik, K. Słabkowska, J. Rzadkiewicz, K. Kozioł, J. Starosta, E. Wiatrowska-Kozioł, J.-C. Dousse, and J. Hoszowska, Phys. Rev. Lett. **107**, 073001 (2011).

[47] K. Kozioł and J. Rzadkiewicz, Phys. Rev. A **96**, 031402 (2017).

[48] B. J. McKenzie, I. P. Grant, and P. H. Norrington, Comput. Phys. Commun. **21**, 233 (1980).

[49] J. A. Lowe, C. T. Chantler, and I. P. Grant, Radiat. Phys. Chem. **85**, 118 (2013).

[50] P. J. Mohr and Y.-K. Kim, Phys. Rev. A **45**, 2727 (1992).

[51] L. W. Fullerton and G. A. Rinker, Phys. Rev. A **13**, 1283 (1976).

[52] C. Froese Fischer, J. Phys. B: At., Mol. Opt. Phys. **43**, 074020 (2010).

[53] C. Froese Fischer, J. Phys. B: At., Mol. Opt. Phys. **44**, 125001 (2011).

[54] J. A. Lowe, C. T. Chantler, and I. P. Grant, Phys. Lett. A **374**, 4756 (2010).

[55] C. Froese Fischer, Relativistic Variational Calculations for Complex Atoms, in *Advances in the Theory of Atomic and Molecular Systems*, edited by P. Piecuch, J. Maruani, G. Delgado-Barrio, and S. Wilson, Progress in Theoretical Chemistry and Physics Vol. 19 (Springer Netherlands, Dordrecht, 2009), pp. 115–128.

[56] J. Clementson, P. Beiersdorfer, G. V. Brown, and M. F. Gu, Phys. Scr. **81**, 015301 (2010).

[57] N. Tragin, J.-P. Geindre, P. Monier, J.-C. Gauthier, C. Chenais-Popovics, J.-F. Wyart, and C. Bauche-Arnoult, Phys. Scr. **37**, 72 (1988).

[58] G. Osborne, A. Safronova, V. Kantsyrev, U. Safronova, P. Beiersdorfer, K. Williamson, M. Weller, and I. Shrestha, Can. J. Phys. **89**, 599 (2011).

[59] H. Bruhns, J. Braun, K. Kubiček, J. R. Crespo López-Urrutia, and J. Ullrich, Phys. Rev. Lett. **99**, 113001 (2007).

[60] P. Indelicato and J.-P. Desclaux, *MCDFGME, a Multiconfiguration Dirac–Fock and General Matrix Elements Program* (release 2005), http://dirac.spectro.jussieu.fr/mcdf.

[61] W. C. Martin and R. Zalubas, J. Phys. Chem. Ref. Data **12**, 323 (1983).

[62] M. Sanchez del Rio, C. Ferrero, and V. Mocella, Proc. SPIE **3151**, 312 (1997).

[63] L.-G. Eriksson, E. Righi, and K.-D. Zastrow, Plasma Phys. Control. Fusion **39**, 27 (1997).

[64] M. F. F. Nave, L.-G. Eriksson, C. Giroud, T. J. Johnson, K. Kirov, M.-L. Mayoral, J.-M. Noterdaeme, J. Ongena, G. Saibene, R. Sartori, F. Rimini, T. Tala, P. de Vries, K.-D. Zastrow, and J.-E. Contributors, Plasma Phys. Control. Fusion **54**, 074006 (2012).

[65] L.-G. Eriksson, T. Hellsten, M. F. F. Nave, J. Brzozowski, K. Holmström, T. Johnson, J. Ongena, K.-D. Zastrow, and J.-E. Contributors, Plasma Phys. Control. Fusion **51**, 044008 (2009).

[66] U. I. Safronova, C. Namba, I. Murakami, W. R. Johnson, and M. S. Safronova, Phys. Rev. A **64**, 012507 (2001).

[67] E. V. Aglitskii, E. P. Ivanova, S. A. Panin, U. I. Safronova, S. I. Ulityn, L. A. Vainshtein, and J.-F. Wyart, Phys. Scr. **40**, 601 (1989).

[68] J. E. Rice, K. Fournier, J. A. Goetz, E. S. Marmar, and J. L. Terry, J. Phys. B: At., Mol. Opt. Phys. **33**, 5435 (2000).

[69] M. Klapisch, J. L. Schwob, B. S. Fraenkel, and J. Oreg, J. Opt. Soc. Am. **67**, 148 (1977).

[70] R. D. Cowan, *The Theory of Atomic Structure and Spectra* (University of California Press, Berkeley 1981).

Correction: In the front matter, the first two affiliations were presented incorrectly during the production process and have been reset properly.